AIAA JOURNAL
Vol. 39, No. 5, May 2001

Adaptive Nonlinear Artificial Dissipation Model for Computational Aeroacoustics

Jae Wook Kim* and Duck Joo Lee†
Korea Advanced Institute of Science and Technology, Taejon 305-701, Republic of Korea

An adaptive nonlinear artificial dissipation model is presented for performing aeroacoustic computations by high-order and high-resolution numerical schemes based on central finite differences. It consists of a selective background smoothing term and a well-established nonlinear shock-capturing term, which damps out spurious oscillations caused by the central differences in the presence of a shock wave and keeps the linear acoustic waves relatively unaffected. A conservative form of the selective background smoothing term is presented to calculate accurate propagation speed or location of the shock wave. The nonlinear shock-capturing term, which has been modeled by second-order derivative term, is combined with it to improve the resolution of discontinuity and enhance the numerical stability near the shock wave. An adaptive control constant for overall amplitude of the dissipation is automatically calculated according to given grid metrics and time-dependent flow conditions. It is shown that the improved artificial dissipation model reproduces the correct profile and speed of the shock wave, suppresses numerical oscillations near the discontinuity, and avoids unnecessary damping on the smooth linear acoustic waves. The feasibility and performance of the adaptive nonlinear artificial dissipation model for the computational aeroacoustics are investigated and validated by the applications to actual problems.

I. Introduction

THE high-order and high-resolution numerical schemes have been developed so far on the basis of central finite differences for computational aeroacoustics (CAA) and used effectively for the generation, propagation, radiation, and scattering of the linear waves.[1–5] They are properly formulated to be less dissipative and dispersive than the other low-order standard schemes. They can reproduce the wave profile and speed accurately using less than only three or four grid points per wavelength. On the other hand, it has been generally recognized that they are less suitable for computations of the nonlinear wave solutions, especially when a discontinuity such as a shock or contact surface is present. Nonlinearity causes the wave profile of an acoustic pulse to steepen and ultimately to form a shock. It was found that the nonlinear wave steepening process, when viewed in the wave number domain, corresponds to an energy cascade process whereby low wave number components are transferred into high wave number range.[6] When a shock is formed, the central differences generally produce spurious spatial oscillations near the shock where a strong discontinuity exists. These oscillations, that is, numerical waves, arise from the unresolved high wave number components generated by the nonlinear cascading process. If the high-order and high-resolution schemes based on the central differences are used for the nonlinear computation without an artificial dissipation model, the computed nonlinear wave profile remains accurate as long as the cascading process does not transfer wave components into the unresolved narrow band of high wave number range.

Several kinds of artificial dissipation models were developed in the aerodynamic sense for the purpose of obtaining numerical stability and fast convergence features of numerical schemes based on the central differences.[7–11] These present good resolution characteristics near the shock wave, but have a tendency to damp out the linear waves seriously because they were originally designed to suppress the low wave number components of a wave profile. Therefore, they are not suited for time-accurate numerical solutions of aeroacoustic problems that contain the linear waves of very small amplitudes in the far field. Jameson et al.,[7] Jameson,[8] Pulliam and Steger,[9] Pulliam,[10] and others[11] applied the nonlinear artificial dissipation model to the steady Euler computations, which was a blend of the second- and fourth-order derivative terms with the nonlinear switching coefficients. It has excellent shock-capturing properties and helps with fast convergence to steady state, but it leads to unnecessary damping on the linear waves because it cannot distinguish the small-amplitude linear waves from the spurious numerical oscillations. Meanwhile, the artificial selective damping model was introduced by Tam et al.[12] and Tam and Shen[13] in the aeroacoustic sense to solve the nonlinear wave problems using the dispersion-relation-preserving scheme,[5] which is the high-order and high-resolution scheme based on the central differences. The artificial selective damping model has been used for time-dependent CAA solutions as well as steady-state mean solutions without a shock wave in the flow. It was designed to damp out the spurious wave components effectively in the high wave number range unresolved by the dispersion-relation-preserving scheme, while at the same time keeping the wave components in the low wave number range nearly unaffected. It is good for both the linear and nonlinear waves without a strong shock; however, it seems to lack the shock-capturing property and make remarkable oscillations near the shock, compared with the previous artificial dissipation models. Lately, Lockhard and Morris[14] further modified the Jameson et al.[7] model to include nonlinear switches in the Tam et al.[12] model, and validated their approach within the multigrid framework for two- and three-dimensional steady-state problems.

In this paper, an improved artificial dissipation model is derived for CAA, which effectively removes the spurious numerical oscillations produced near the shock wave but hardly affects the linear acoustic waves. The artificial selective damping model and the nonlinear artificial dissipation model are combined for the numerical stability and temporal accuracy of CAA performed by the high-order and high-resolution central difference schemes. The artificial selective damping model is reformulated into a conservative form to maintain correct location or propagation speed of the shock wave.[15] The second-order derivative term in the nonlinear artificial dissipation model is combined with the artificial selective damping model to improve the shock-capturing property progressively. Multidimensional formalism is presented in the generalized coordinates for applications to practical problems with complex geometry. An adaptive control constant is devised to adjust the local level of the dissipation magnitude automatically, according to flow conditions and grid meshes. Performance of the adaptive nonlinear artificial

Received 20 January 2000; revision received 8 July 2000; accepted for publication 21 July 2000.

*Graduate Student, Department of Aerospace Engineering; currently Postdoctoral Research Associate, Department of Aerospace Engineering, 373-1 Kusong-dong, Yusong-gu.

†Professor, Department of Aerospace Engineering, 373-1 Kusong-dong, Yusong-gu. Member AIAA.

dissipation model presented in this paper is tested and compared with the previous models by applying it to simple one-dimensional problems of the linear and nonlinear wave propagation that have exact solutions. It is also applied to quasi-one- and two-dimensional computations of shock–sound interaction in a transonic nozzle to validate its performance in more general and complex cases. The compressible Euler equations in entire conservation form are solved for the present computations. The optimized fourth-order compact schemes[1–3] are used for evaluation of the spatial derivatives, and the classical fourth-order Runge–Kutta scheme is used for temporal integration of the solutions. The feasibility of the adaptive nonlinear artificial dissipation model is investigated for CAA.

II. Governing Equations

The unsteady compressible Euler equations in entire conservation form are considered in the formulations of the artificial dissipation models and their applications to actual computations in the present work. One-dimensional equations in Cartesian coordinates, quasi-one- and two-dimensional equations in the generalized coordinates are provided as follows.

A. One-Dimensional Equations

The one-dimensional equations in Cartesian coordinates are expressed in a flux vector form as

$$\frac{\partial \boldsymbol{Q}}{\partial t} + \frac{\partial \boldsymbol{E}}{\partial x} = \boldsymbol{0} \tag{1}$$

where $\boldsymbol{Q} = [\rho,\ \rho u,\ \rho e_t]^T$ is the vector of conservative variables and $\boldsymbol{E} = [\rho u,\ \rho u^2 + p,\ (\rho e_t + p)u]^T$ is the inviscid flux vector. Of the dependent variables, ρ is density, p is pressure, u is velocity, and e_t is total internal energy defined as $e_t = p/[(\gamma - 1)\rho] + u^2/2$.

B. Quasi-One-Dimensional Equations

The quasi-one-dimensional equations in the generalized coordinates are expressed in a flux vector form as

$$\frac{\partial (A\hat{\boldsymbol{Q}})}{\partial t} + \frac{\partial (A\hat{\boldsymbol{E}})}{\partial \xi} - \hat{\boldsymbol{H}} = \boldsymbol{0} \tag{2}$$

where $\hat{\boldsymbol{Q}} = \boldsymbol{Q}/J$ is the vector of conservative variables, $\hat{\boldsymbol{E}} = \xi_x \boldsymbol{E}/J$ is the inviscid flux vector, and $\hat{\boldsymbol{H}} = \xi_x A_\xi [0,\ p,\ 0]^T/J$ is the source vector in the generalized coordinate system. $A = A(x)$ is the cross-sectional area. The superscript $\hat{}$ denotes the functions in the generalized coordinates system. J is the transformation Jacobian, and ξ_x is the transformation metric from the Cartesian to the generalized coordinates. In this case, J is identical to ξ_x.

C. Two-Dimensional Equations

For a practical computation in a domain with complex geometry or boundaries, it is necessary to utilize the multidimensional equations that are transformed from a physical space with Cartesian coordinates to a computational space with the generalized coordinates. The two-dimensional equations in the generalized coordinates are expressed in a flux vector form as

$$\frac{\partial \hat{\boldsymbol{Q}}}{\partial t} + \frac{\partial \hat{\boldsymbol{E}}}{\partial \xi} + \frac{\partial \hat{\boldsymbol{F}}}{\partial \eta} = \boldsymbol{0} \tag{3}$$

where $\hat{\boldsymbol{Q}} = [\rho, \rho u, \rho v, \rho e_t]^T/J$ is the vector of conservative variables and the inviscid flux vectors are

$$\hat{\boldsymbol{E}} = [\rho U,\ \rho u U + \xi_x p,\ \rho v U + \xi_y p,\ (\rho e_t + p)U]^T \Big/ J$$

$$\hat{\boldsymbol{F}} = [\rho V,\ \rho u V + \eta_x p,\ \rho v V + \eta_y p,\ (\rho e_t + p)V]^T \Big/ J$$

The superscript $\hat{}$ denotes the functions in the generalized coordinates system. J is the transformation Jacobian and ξ_x, ξ_y, η_x, and η_y are the transformation metrics from Cartesian to the generalized coordinates in two dimensions. The contravariant velocities are expressed as $U = \xi_x u + \xi_y v$ and $V = \eta_x u + \eta_y v$. The total internal energy is $e_t = p/[(\gamma - 1)\rho] + (u^2 + v^2)/2$ in two dimensions.

III. Previous Artificial Dissipation Models

It has been shown that the artificial dissipation models introduce an upwind correction to the central difference schemes to remove nonphysical effects arising from the central discretization of wave propagation phenomena.[7–11] These effects arise mainly around the discontinuity, where a sudden change in the propagation direction of the nonlinear waves occurs. Because of its nature, the central discretization is not able to handle this discontinuous change and generates oscillations. Therefore, in early works, the artificial dissipation models had been developed to remove the spurious oscillations for the robustness of stability and the fast convergence of solutions in the steady-state aerodynamic sense. Recently, the focus of the artificial dissipation model was changed to accurate computations of unsteady aerodynamics in the near field and, especially, acoustics in the far field.

A. Nonlinear Artificial Dissipation Model

The typical artificial dissipation or viscosity models have been developed so far for the purpose of fast convergence to steady-state solutions without numerical oscillations around a shock wave. These additional terms should simulate the effects of physical viscosity on the scale of grid mesh locally around the shock wave and be negligible, which is of an order equal or higher than the truncation error, in smooth regions. Jameson et al.[7] have employed the nonlinear artificial dissipation model that consists of the second- and fourth-order derivative terms with an excellent shock-capturing property. In this approach, the fourth-order derivative term is switched off when the pressure gradient dominates. Consider one-dimensional equations of fluid motion [i.e., compressible Euler equations (1) discretized on a uniform grid mesh with spacing Δx], where the dissipation terms are added to the right-hand side of the equations. At the ith grid point, the Euler equation with the nonlinear artificial dissipation term $\boldsymbol{D}_i$ can be written as

$$\left.\frac{\partial \boldsymbol{Q}}{\partial t}\right|_i + \left.\frac{\partial \boldsymbol{E}}{\partial x}\right|_i = \boldsymbol{D}_i \tag{4}$$

The artificial dissipation term $\boldsymbol{D}_i$ is represented by the difference of a numerical dissipation flux vector $\boldsymbol{d}_i$:

$$\boldsymbol{D}_i = \left(\boldsymbol{d}_{i+\frac{1}{2}} - \boldsymbol{d}_{i-\frac{1}{2}}\right)\Big/ \Delta x \tag{5}$$

$$\boldsymbol{d}_{i+\frac{1}{2}} = |\lambda|_{i+\frac{1}{2}} \Big[\varepsilon^{(2)}_{i+\frac{1}{2}} (\boldsymbol{Q}_{i+1} - \boldsymbol{Q}_i) - \varepsilon^{(4)}_{i+\frac{1}{2}} (\boldsymbol{Q}_{i+2} - 3\boldsymbol{Q}_{i+1} + 3\boldsymbol{Q}_i - \boldsymbol{Q}_{i-1}) \Big] \tag{6}$$

Equation (6) expresses the combination of the second- and fourth-order derivative terms with local nonlinear dissipation functions and absolute eigenvalue. The absolute eigenvalue and its midpoint value are as follows:

$$|\lambda|_i = (|u| + c)_i, \qquad |\lambda|_{i+\frac{1}{2}} = \tfrac{1}{2}(|\lambda|_i + |\lambda|_{i+1}) \tag{7}$$

where c is the speed of sound. The nonlinear dissipation function $\varepsilon^{(2)}$ and its midpoint value are evaluated as

$$\varepsilon^{(2)}_i = \kappa^{(2)} \frac{|p_{i+1} - 2p_i + p_{i-1}|}{p_{i+1} + 2p_i + p_{i-1}}, \qquad \varepsilon^{(2)}_{i+\frac{1}{2}} = \max\left(\varepsilon^{(2)}_i, \varepsilon^{(2)}_{i+1}\right) \tag{8}$$

where $\kappa^{(2)}$ is an adjustable constant. The pressure term in $\varepsilon^{(2)}$ is generally of the second order except in regions of strong pressure gradients, where it reduces to first order. Hence, around a shock wave, the $\varepsilon^{(2)}$ term is dominating. This did not appear to be sufficient to avoid some small oscillations, of the order of 1% in density variation, which prevented complete convergence to the steady state. These oscillations were removed by introducing the fourth-order derivative term, which provided some background dissipation through the domain, but led to the reappearance of overshoots around the shock

wave. Therefore, the background dissipation is turned off when $\varepsilon^{(2)}$ is large and one defines

$$\varepsilon^{(4)}_{i+\frac{1}{2}} = \max\left[0, \left(\kappa^{(4)} - \varepsilon^{(2)}_{i+\frac{1}{2}}\right)\right] \tag{9}$$

where $\kappa^{(4)}$ is an adjustable constant. The typical values of $\kappa^{(2)} = \frac{1}{2}$ and $\kappa^{(4)} = \frac{1}{100}$ suggested by Jameson et al.[7] are used for optimal results in the present computations. This model has an excellent shock-capturing property and gives sufficient numerical stability to the central difference schemes. However, it was not designed for the time-dependent solutions of the aeroacoustic problems. Excessive dissipation occurs in the low-wave-number range, and the linear acoustic waves can be suppressed seriously.

B. Artificial Selective Damping Model

To obtain a high-quality numerical solution, it is necessary to eliminate the spurious numerical wave components unresolved in the narrow band of the high-wave-number range, while at the same time keeping the wave components well-resolved in the wideband of the low-wave-number range unaffected. This can be achieved by inserting the artificial selective damping term introduced by Tam et al.[12] in the finite difference equations. It is constructed in the seven-point stencil as suggested in Refs. 12 and 13, and it can be written here as

$$\boldsymbol{D}_i = -\frac{\nu_a}{(\Delta x)^2} \sum_{m=-3}^{3} a_m \boldsymbol{Q}_{i+m} \tag{10}$$

where ν_a is the variable artificial viscosity to adjust the magnitude of damping and a_m are the damping coefficients. The damping coefficients a_m are determined by the Fourier analysis in the wave number domain. By choosing the coefficients properly, it can be possible to make the damping occur only in the narrow band of the high-wave-number range. The way to optimize them is represented precisely in Refs. 2, 12, and 13. The authors suggest the following coefficients:

$$a_0 = 0.3248765149154926$$

$$a_1 = a_{-1} = -0.2355295710360009$$

$$a_2 = a_{-2} = 0.0875617425422537 1$$

$$a_3 = a_{-3} = -0.0144704289639991 5$$

The variable artificial viscosity was defined as $\nu_a = u_i^{\text{stencil}} \Delta x / Re_a$, where the stencil velocity is

$$u_i^{\text{stencil}} = \max_{m=-3}^{3} (u_{i+m}) - \min_{m=-3}^{3} (u_{i+m}) \tag{11}$$

Then the artificial selective damping term is rewritten as

$$\boldsymbol{D}_i = -\frac{u_i^{\text{stencil}}}{Re_a \Delta x} \sum_{m=-3}^{3} a_m \boldsymbol{Q}_{i+m} \tag{12}$$

The stencil velocity is for measuring the velocity gradient or shock strength in the seven-point stencil, and Re_a is the artificial Reynolds number to determine the overall magnitude of damping. The typical value of $Re_a = 0.05$ suggested by Tam et al.[12] is used for optimal results in the present computations. The stencil velocity defined in Eq. (11) is a function of space, whose value varies with the grid points. It is not contained in the difference operator as shown in Eq. (12); thus, it may cause a nonconservative feature, which can create some error in computing the location or propagation speed of a shock wave as reported in Ref. 15. The artificial selective damping model is good for suppressing the undesirable spurious oscillations in the entire computational domain. However, it cannot help generating remarkable oscillations locally when it meets a shock wave because it has no shock-capturing term to be switched on in such a case. The amplitude of these oscillations does not seem so high; however, in aeroacoustic point of view, they can result in a serious problem that must be handled carefully.

IV. Adaptive Nonlinear Artificial Dissipation (ANAD) Model

A typical artificial dissipation model consists of the second- and fourth-order derivative terms in conservative form. One is for the shock capturing and the other is for the background smoothing effect; however, the effect of the background smoothing term is so excessive that it may seriously damp out the linear acoustic waves, and it is not proper for CAA. On the other hand, the artificial selective damping model lacks the shock-capturing property and still produces considerable numerical oscillations near a shock wave. Moreover, it was proposed in a nonconservation form, and so it may have some error in computing the location or propagation speed of the shock wave if it is used in the original form.[15] In this paper, a revised formulation of the artificial selective damping term in a conservative form is presented. Then, it is desirable to combine the shock-capturing term and the artificial selective damping term as the background smoothing term. In this paper, this combination supported by an adaptive control constant and nonlinear switching functions is proposed as an adaptive nonlinear artificial dissipation (ANAD) model.

A. Conservative Formulation of Background Smoothing Term

It is required to confine the variable, which is a function of space, within the difference operator to construct a conservative formulation. In Eq. (12), the stencil velocity is out of the damping operator, and the form is not conservative yet. Therefore, the damping operator should be changed into a form of difference between two split damping flux terms where each flux term includes the stencil velocity. Then the background smoothing term is represented in the flux difference form as

$$\boldsymbol{D}_i = \left(\boldsymbol{d}_{i+\frac{1}{2}} - \boldsymbol{d}_{i-\frac{1}{2}}\right) \Big/ \Delta x \tag{13}$$

where the damping flux vector $\boldsymbol{d}_i$ is given as

$$\boldsymbol{d}_{i+\frac{1}{2}} = C_{i+\frac{1}{2}} \sum_{m=-2}^{3} b_m \boldsymbol{Q}_{i+m} \tag{14}$$

and $C_{i+1/2}$ is a controlling function of dissipation magnitude at the interface of adjacent two cells. It is given as $C_{i+1/2} = -u^{\text{stencil}}_{i+1/2}/Re_a$ for the Tam et al.[12] model described in Eq. (12), and it is changed to an improved one for the ANAD model in this paper as will be shown in the next subsections. Equation (13) is of the flux difference form, and all of the space functions are confined within each flux term, that is, the conservative form is achieved. The damping coefficients b_m are determined by some arithmetic relations matching with the coefficients a_m in Eq. (12). The matching condition makes Eq. (13) equal to Eq. (12) when the stencil velocity is locally a constant, and it is represented as

$$\sum_{m=-2}^{3} b_m \boldsymbol{Q}_{i+m} - \sum_{m=-2}^{3} b_m \boldsymbol{Q}_{(i-1)+m} = \sum_{m=-3}^{3} a_m \boldsymbol{Q}_{i+m} \tag{15}$$

Equation (15) should be satisfied independently of the location or the index i of the grid points. In this course, the following relation is derived:

$$b_m = \sum_{n=m}^{3} a_n \qquad (m = -3, \ldots, 2)$$

then the new damping coefficients are obtained as follows:

$$b_1 = -b_0 = -0.1624382574577463$$

$$b_2 = -b_{-1} = 0.0730913135782545 5$$

$$b_3 = -b_{-2} = -0.0144704289639991 5$$

By the use of these coefficients, the conservative formulation of the artificial selective damping model is achieved, which is used as

the background smoothing term in the present paper. The effect of conservative formulation is compared with that of nonconservative formulation by applying it to an actual computation in Sec. V.

B. One-Dimensional Formulation of ANAD Model

The ANAD model is presented by combining the shock-capturing term in Eq. (6) and the background smoothing term of Eq. (14) with modified nonlinear dissipation functions. One-dimensional formalism of the ANAD model is suggested in Cartesian coordinates. Consider the dissipation term $\boldsymbol{D}_i$ included in Eq. (1) at the ith grid point as expressed in Eq. (4), where the dissipation term is represented in the conservative form as

$$\boldsymbol{D}_i = \left(\boldsymbol{d}_{i+\frac{1}{2}} - \boldsymbol{d}_{i-\frac{1}{2}}\right)\Big/\Delta x \tag{16}$$

which is the same as Eq. (5) and (13), whereas the numerical dissipation flux vector is revised in this paper as

$$\begin{aligned}\boldsymbol{d}_{i+\frac{1}{2}} &= |\lambda|^{\text{stencil}}_{i+\frac{1}{2}}\left[\varepsilon^{(2)}_{i+\frac{1}{2}}(\boldsymbol{Q}_{i+1}-\boldsymbol{Q}_i) - \varepsilon^{(4)}_{i+\frac{1}{2}}\sum_{m=-2}^{3} b_m \boldsymbol{Q}_{i+m}\right]\\ &= |\lambda|^{\text{stencil}}_{i+\frac{1}{2}}\left\{\varepsilon^{(2)}_{i+\frac{1}{2}}(\boldsymbol{Q}_{i+1}-\boldsymbol{Q}_i) - \varepsilon^{(4)}_{i+\frac{1}{2}}[b_1(\boldsymbol{Q}_{i+1}-\boldsymbol{Q}_i)\right.\\ &\left. + b_2(\boldsymbol{Q}_{i+2}-\boldsymbol{Q}_{i-1}) + b_3(\boldsymbol{Q}_{i+3}-\boldsymbol{Q}_{i-2})]\right\}\end{aligned} \tag{17}$$

Equations (16) and (17) express the combination of the second- and fourth-order derivative terms with the local nonlinear dissipation functions and the stencil eigenvalue. The stencil eigenvalue is evaluated on the midpoint just like the stencil velocity in Eq. (14), and it is used as a shock or discontinuity detector using the eigenvalues. It is represented as

$$|\lambda|^{\text{stencil}}_{i+\frac{1}{2}} = \max_{m=-2}^{3}(|\lambda|_{i+m}) - \min_{m=-2}^{3}(|\lambda|_{i+m}) \tag{18}$$

where the absolute eigenvalue is defined in Eq. (7). The nonlinear dissipation functions $\varepsilon^{(2)}_{i+1/2}$ and $\varepsilon^{(4)}_{i+1/2}$ in Eq. (17) determine the magnitudes of the second- and fourth-order dissipation according to the change of pressure gradient. In regions of strong discontinuity, the second-order dissipation, that is, the shock-capturing term, dominates, and the fourth-order one is turned off. Out of the region, the second-order one becomes a very small value and the fourth-order one, that is, the background smoothing term, governs the dissipation. The nonlinear dissipation functions are suggested in this paper as

$$\varepsilon^{(2)}_{i+\frac{1}{2}} = \kappa \max_{m=-2}^{3}(\nu_{i+m}), \qquad \varepsilon^{(4)}_{i+\frac{1}{2}} = \max\left[0, \left(\kappa - \varepsilon^{(2)}_{i+\frac{1}{2}}\right)\right] \tag{19}$$

where the pressure shock detector is given as $\nu_i = |p_{i-1} - 2p_i + p_{i+1}|/(p_{i-1} - 2p_i + p_{i+1})$. Equation (19) is extended from Eq. (8) for the purpose of having an effect on the wide stencil of the high-order and high-resolution schemes in the present paper. The variables placed out of boundaries in Eqs. (17–19) can be extrapolated by the values on interior points. A standard fourth-order extrapolation function is used to minimize unnecessary background dissipation near and at the boundaries, keeping in mind that the background smoothing term is a model of the fourth-order derivatives. This kind of extrapolation also applies to the next subsections.

The adaptive control constant κ is devised in this paper to determine the magnitude of dissipation level in entire domain, and this is automatically adjusted according to the flow conditions or grid meshes. The adaptive control constant is evaluated as

$$\kappa = (1/\sigma^{1/\alpha})\{[(\alpha+1)/(\alpha-1)]\tanh(\alpha-1)\}^{1+\tanh(\sigma-1)} \tag{20}$$

where $\sigma = p^{\max}/p^{\min}$ and $\alpha = |\lambda|^{\max}/|\lambda|^{\min}$. The superscripts max and min imply the maximum and minimum values of a variable along a grid line, respectively, which are expressed as

$$f^{\max} = \max_{i=0}^{i\,\max} f_i, \qquad f^{\min} = \min_{i=0}^{i\,\max} f_i \tag{21}$$

If there is a chance of having the value of α equal to unity, which causes a numerical singularity in Eq. (20), one can avoid such an instability simply by adding a small number (1×10^{-8} or less) to the denominator. The adaptive control constant expressed in Eq. (20) is newly suggested in this paper for effective applications of the artificial dissipation model to various CAA problems, which can be used for the linear and nonlinear waves simultaneously. The authors found out that optimal values of the control constant on uniform grids are inversely proportional to the factor $\sigma^{1/\alpha}$ through investigations for various flow conditions. The weighting function in the square brackets is devised to maintain some finite level of dissipation when the flow is almost uniform [α approaches unity and the stencil eigenvalue in Eq. (18) approaches zero] and to avoid excessive dissipation when the flow is severe (α and the stencil eigenvalue become large). The exponent is a correction factor of the weighting function according to σ, which becomes unity when the flow is uniform and becomes double when the flow is severe. At each time step, an optimal value of the control constant is calculated automatically by the flow properties. One need not readjust it case by case or waste additional computation time tuning the value. It will become very useful when proven to still be effective after more applications to various problems by many users hereafter.

C. Quasi-One-Dimensional Formulation of ANAD Model

Quasi-one-dimensional formalism of the ANAD model is suggested in the generalized coordinates. Consider the dissipation term added on the right-hand side of the quasi-one-dimensional Euler equations expressed by Eq. (2) at the ith grid point:

$$\left.\frac{\partial(A\hat{\boldsymbol{Q}})}{\partial t}\right|_i + \left.\frac{\partial(A\hat{\boldsymbol{E}})}{\partial \xi}\right|_i - \hat{\boldsymbol{H}}_i = \hat{\boldsymbol{D}}_i \tag{22}$$

where the dissipation term $\hat{\boldsymbol{D}}_i$ is given as

$$\hat{\boldsymbol{D}}_i = \left(A_{i+\frac{1}{2}}\hat{\boldsymbol{d}}_{i+\frac{1}{2}} - A_{i-\frac{1}{2}}\hat{\boldsymbol{d}}_{i-\frac{1}{2}}\right)\Big/\Delta\xi \tag{23}$$

Then the numerical dissipation flux vector in the generalized coordinates is given as

$$\begin{aligned}\hat{\boldsymbol{d}}_{i+\frac{1}{2}} &= \frac{|\lambda|^{\text{stencil}}_{i+\frac{1}{2}}}{J_{i+\frac{1}{2}}}\left[\varepsilon^{(2)}_{i+\frac{1}{2}}(\boldsymbol{Q}_{i+1}-\boldsymbol{Q}_i) - \varepsilon^{(4)}_{i+\frac{1}{2}}\sum_{m=-2}^{3} b_m \boldsymbol{Q}_{i+m}\right]\\ &= \frac{|\lambda|^{\text{stencil}}_{i+\frac{1}{2}}}{J_{i+\frac{1}{2}}}\left\{\varepsilon^{(2)}_{i+\frac{1}{2}}(\boldsymbol{Q}_{i+1}-\boldsymbol{Q}_i) - \varepsilon^{(4)}_{i+\frac{1}{2}}[b_1(\boldsymbol{Q}_{i+1}-\boldsymbol{Q}_i)\right.\\ &\left. + b_2(\boldsymbol{Q}_{i+2}-\boldsymbol{Q}_{i-1}) + b_3(\boldsymbol{Q}_{i+3}-\boldsymbol{Q}_{i-2})]\right\}\end{aligned} \tag{24}$$

The cross-sectional area on the midpoint in Eq. (23) and the transformation Jacobian on the midpoint in Eq. (24) are evaluated by the arithmetic averages of the values on the adjacent two grid points as $A_{i+1/2} = (A_{i+1} + A_i)/2.$ and $J_{i+1/2} = (J_{i+1} + J_i)/2.$ The stencil eigenvalue, $|\lambda|^{\text{stencil}}_{i+1/2}$ is also evaluated by Eq. (18) in this case, where the absolute eigenvalue is defined differently compared with Eq. (7) in the generalized coordinates as $|\lambda|_i = (|u| + c)_i|\xi_x|_i$. The nonlinear dissipation functions $\varepsilon^{(2)}_{i+1/2}$ and $\varepsilon^{(4)}_{i+1/2}$ and the shock detector ν_i are the same as those of the one-dimensional case.

The adaptive control constant in the generalized coordinates is also devised as

$$\kappa = (1/\sigma^R)[1 + (\sigma-1)\tanh(\alpha/\beta - 1)]\left(\sqrt{\hat{\alpha}\hat{\beta}}\right)^{1+\tanh(\sigma-1)} \tag{25}$$

where σ and α are the same as those of the one-dimensional case and the other functions are additionally defined as

$$\beta = \frac{(|\lambda|/|\xi_x|)^{\max}}{(|\lambda|/|\xi_x|)^{\min}}, \qquad R = \frac{(\alpha+\beta)}{(2\alpha\beta)}$$

$$\hat{\alpha} = \left[\frac{(\alpha+1)}{(\alpha-1)}\right]\tanh(\alpha-1)$$

$$\hat{\beta} = \left[\frac{(\beta+1)}{(\beta-1)}\right]\tanh(\beta-1)$$

In this case, α and $\hat{\alpha}$ are functions of the eigenvalue in the generalized coordinates, and β and $\hat{\beta}$ are those in Cartesian coordinates. The superscripts max and min are explained by Eq. (21). Equation (25) is extended from Eq. (20) for using on nonuniform grids and, therefore, becomes the same as Eq. (20) when used on uniform grids where $\alpha = \beta$, $\hat{\alpha} = \hat{\beta}$, and $R = 1/\alpha$. The authors found through many of investigations on various nonuniform grid meshes that an additional factor expressed in the square brackets of Eq. (25) is needed for the control constant in the generalized coordinates, which becomes proportional to σ when α/β is large enough. The function R is just the arithmetic average of $1/\alpha$ and $1/\beta$, and the function in the third parentheses of Eq. (25) is just the geometric average of $\hat{\alpha}$ and $\hat{\beta}$, which are devised to take into account both the Cartesian and the generalized coordinates properties.

D. Two-Dimensional Formulation of ANAD Model

For a practical computation in a domain with a complex geometry of boundaries, it is necessary to utilize the multidimensional equations, which are transformed from a physical space with Cartesian coordinates to a computational space with generalized coordinates. Two-dimensional formalism of the ANAD model is suggested in the generalized coordinates. Consider the dissipation model added on the right-hand side of the two-dimensional Euler equations expressed by Eq. (3), where the dissipation model is divided into two terms in the ξ and η directions. The equations with the two ANAD terms are written at the (i, j)th grid point as

$$\left.\frac{\partial \hat{\boldsymbol{Q}}}{\partial t}\right|_{i,j} + \left.\frac{\partial \hat{\boldsymbol{E}}}{\partial \xi}\right|_{i,j} + \left.\frac{\partial \hat{\boldsymbol{F}}}{\partial \eta}\right|_{i,j} = \hat{\boldsymbol{D}}^{\xi}_{i,j} + \hat{\boldsymbol{D}}^{\eta}_{i,j} \tag{26}$$

where $\hat{\boldsymbol{D}}^{\xi}_{i,j}$ is the dissipation term in the ξ direction and $\hat{\boldsymbol{D}}^{\eta}_{i,j}$ is that in the η direction. The ANAD term in the ξ direction is represented in the finite difference form as

$$\hat{\boldsymbol{D}}^{\xi}_{i,j} = \left(\hat{\boldsymbol{d}}^{\xi}_{i+\frac{1}{2},j} - \hat{\boldsymbol{d}}^{\xi}_{i-\frac{1}{2},j}\right) \Big/ \Delta\xi \tag{27}$$

where the numerical dissipation flux is

$$\begin{aligned}\hat{\boldsymbol{d}}^{\xi}_{i+\frac{1}{2},j} = \frac{|\lambda|^{\text{stencil}}_{i+\frac{1}{2},j}}{J_{i+\frac{1}{2},j}} \Big\{ & \varepsilon^{(2)}_{i+\frac{1}{2},j}(\boldsymbol{Q}_{i+1,j} - \boldsymbol{Q}_{i,j}) \\ & + \varepsilon^{(4)}_{i+\frac{1}{2},j}[b_1(\boldsymbol{Q}_{i+1,j} - \boldsymbol{Q}_{i,j}) + b_2(\boldsymbol{Q}_{i+2,j} - \boldsymbol{Q}_{i-1,j}) \\ & + b_3(\boldsymbol{Q}_{i+3,j} - \boldsymbol{Q}_{i-2,j})]\Big\}\end{aligned} \tag{28}$$

The two-dimensional stencil eigenvalue is defined as

$$|\lambda|^{\text{stencil}}_{i+\frac{1}{2},j} = \max_{m=-2}^{3}(|\lambda|_{i+m,j}) - \min_{m=-2}^{3}(|\lambda|_{i+m,j}) \tag{29}$$

The two-dimensional absolute eigenvalue is expressed as $|\lambda|_{i,j} = (|U| + c\sqrt{(\xi_x^2 + \xi_y^2)})_{i,j}$ in the generalized coordinates. The two-dimensional transformation Jacobian on the midpoint in Eq. (28) is evaluated as $J_{i+1/2,j} = (J_{i+1,j} + J_{i,j})/2$. The nonlinear dissipation functions in this case are the same as those of the earlier cases but are expressed in two-dimensional notations as

$$\varepsilon^{(2)}_{i+\frac{1}{2},j} = \kappa_j \max_{m=-2}^{3}(\nu_{i+m,j}) \quad \varepsilon^{(4)}_{i+\frac{1}{2},j} = \max\left[\left(\kappa_j - \varepsilon^{(2)}_{i+\frac{1}{2},j}\right), 0\right] \tag{30}$$

where the pressure shock detector is given as

$$\nu_{i,j} = \frac{|p_{i-1,j} - 2p_{i,j} + p_{i+1,j}|}{p_{i-1,j} + 2p_{i,j} + p_{i+1,j}}$$

The adaptive control constant in this case is the same as those of the quasi-one-dimensional case in the generalized coordinates, but is expressed in two-dimensional notation as

$$\kappa_j = \left(1/\sigma_j^{R_j}\right)[1 + (\sigma_j - 1)\tanh(\alpha_j/\beta_j - 1)]\left(\sqrt{\hat{\alpha}_j\hat{\beta}_j}\right)^{1+\tanh(\sigma_j - 1)} \tag{31}$$

where

$$\sigma_j = \frac{p_j^{\max}}{p_j^{\min}}, \qquad \alpha_j = \frac{|\lambda|_j^{\max}}{|\lambda|_j^{\min}}$$

$$\beta_j = \left(\frac{|\lambda|}{\sqrt{\xi_x^2 + \xi_y^2}}\right)_j^{\max} \Bigg/ \left(\frac{|\lambda|}{\sqrt{\xi_x^2 + \xi_y^2}}\right)_j^{\min}$$

$$R_j = \frac{\alpha_j + \beta_j}{2\alpha_j\beta_j}, \quad \hat{\alpha}_j = \left\lfloor \frac{\alpha_j + 1}{\alpha_j - 1} \right\rfloor \tanh(\alpha_j - 1)$$

$$\hat{\beta}_j = \left\lfloor \frac{\beta_j + 1}{\beta_j - 1} \right\rfloor \tanh(\beta_j - 1)$$

The superscripts max and min are expressed in two dimensions as

$$f_j^{\max} = \max_{i=0}^{i\max} f_{i,j}, \qquad f_j^{\min} = \min_{i=0}^{i\max} f_{i,j} \tag{32}$$

All of the preceding functions are already explained in earlier subsections, but are defined here as a list of functions of subscript j in two dimensions.

V. Application to Computations and Validation

In this section, the ANAD model is applied to actual computations of the benchmarking problems, and then its accuracy and performance are validated. A one-dimensional linear wave convection and a shock-tube simulation problem, which have exact solutions, are solved for the comparisons of the present ANAD model and the other models developed previously. Sound wave propagation through a shock in a transonic nozzle is computed as a quasi-one-dimensional problem, and the numerical solutions are compared with the analytic solutions. This problem is also solved in two dimensions to test the multidimensionality of the ANAD model, and the two-dimensional results are also compared with the quasi-one-dimensional analytic solutions. In this course, it is shown that the ANAD model enables the high-order and high-resolution central difference schemes to simulate the shock–sound interactions successfully. The feasibility of the ANAD model for linear and nonlinear CAA is demonstrated.

A. Numerical Schemes and Boundary Conditions

The high-order and high-resolution numerical algorithms developed for CAA are applied to the present computations. The optimized fourth-order compact scheme,[1–3] which is a kind of Padé scheme in a pentadiagonal family, is used for the evaluation of spatial derivatives. The classical fourth-order, four-stage Runge–Kutta scheme is used for the temporal integration of solutions. These schemes resolve a wider band of wave number or frequency range than the other well-established low-order ones. However, because the present schemes do not always effectively resolve the high wave number or frequency range, the ANAD model is introduced to remove the unwanted numerical oscillations that may develop from the unresolved range. The ANAD model is implemented only at the last (fourth) stage of the Runge–Kutta marching to minimize the computational costs due to the dissipation processes.

Besides the stringent requirements on the high-order and high-resolution numerical schemes, an accurate and robust calculation of sounds depends heavily on the suppression of any waves that may result from unwanted reflections on the computational boundaries. Therefore, the boundary conditions for CAA should be physically correct and numerically well posed. The generalized characteristic boundary conditions[16–18] are each used as that kind of time-dependent boundary condition in the present computations. The nonreflecting inflow/outflow conditions and transparent source conditions are implemented on the inlet and exit plane. The slip wall conditions are imposed on the inviscid wall surfaces in the two-dimensional problem.

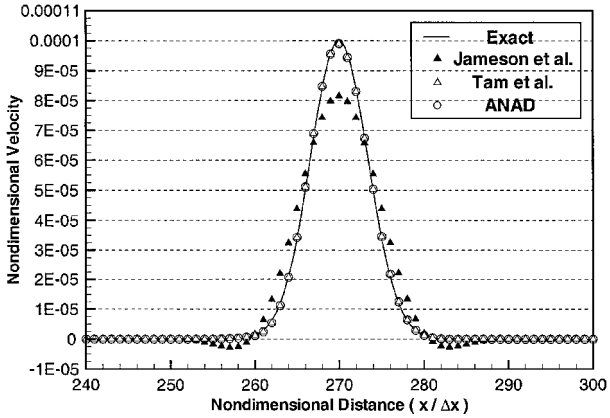

Fig. 1 Computation of linear wave pulse propagation (velocity profile).

B. One-Dimensional Computations

For one-dimensional computations, two kinds of initial-value problems are solved; one is the linear wave pulse propagation and the other is the shock-tube simulation, which were previously discussed in Ref. 19. The one-dimensional Euler equations expressed as Eq. (4) are solved. The computation of the first problem starts from the initial conditions, which consist of the bell-shaped linear pulses of the density, pressure, and velocity, whose magnitudes are 1×10^{-4} times the ambient density, pressure, and sound speed, respectively. The number of grid points used is 401, the time step used is determined by a Courant–Friedrichs–Lewy (CFL) condition with Courant number of 0.9, and the number of operations is 300 for the first problem. The second problem starts from the initial conditions that have the discontinuity at a diaphragm, where the ratio of values before and behind the diaphragm is 10:1 for density and 8.6618:0.5 for pressure. The number of grid points used is 251, the Courant number is also 0.9, and the number of operations is 160 for the second problem. In the computations, the accuracy and effectiveness of the ANAD model are studied and compared with the other models.[7,12] The numerical solutions are represented in comparison with the exact solutions. The results of computations are presented in Figs. 1 and 2.

In Fig. 1, it is shown that the ANAD model has little effect on the linear wave of very small amplitude and retains the wave profile correctly. Similar results are obtained by the Tam et al.[12] model, whereas the Jameson et al.[7] model damps out the linear wave seriously. In Fig. 2, it is shown that the ANAD model captures the strong shock wave and contact surface well without spurious oscillations and that the propagation speed of the shock wave is reproduced correctly, in comparison with exact solutions. The Jameson et al. model creates serious damping on the contact surface. The Tam et al.[12] model lacks the shock-capturing property, produces remarkable oscillations near the shock, and creates a slightly slower shock propagation speed than the others, which is probably caused by its nonconservative form. The ANAD model provides satisfactory results in both the linear and nonlinear cases. The values of adaptive control constant for the ANAD model calculated by Eq. (20) are $\kappa = 2.0$ in Fig. 1 and $\kappa = 1.418$ in Fig. 2.

A formal analysis of accuracy is needed to validate quality of the solutions and effectiveness of the ANAD model. Some quantitative measure (i.e., L_2 norm of the errors deviated from the exact solutions) can be suggested as

$$E = \sqrt{\frac{1}{i\,\max}\sum_{i=0}^{i\,\max}\left(\frac{f_i^{\text{numerical}} - f_i^{\text{exact}}}{f^{\text{exact mean}}}\right)^2}$$

The errors estimated by the preceding equation are listed in Table 1 for the one-dimensional computations, which reveals that the ANAD model provides higher accuracy in both the linear and nonlinear problems than do the previous models.

The nonconservative form of the ANAD model is applied to the second problem to investigate its effects in comparison with the conservative form of the ANAD model. The resulting solutions obtained after 480 operations (three times as many as those for Fig. 2) are presented in Fig. 3, where a section of the whole domain is zoomed in at the shock front area. In Fig. 3, it is clearly shown that the nonconservative form makes remarkable errors in the shock propagation speed and even in the mean amplitude before the shock, as Ref. 15 already reported. The errors become enlarged as the operations continue. The advantage of the conservative form is verified again in the present work.

Table 1 Accuracy comparison in the one-dimensional computations

Cases	Jameson et al.[7]	Tam et al.[12]	ANAD
Linear (Fig. 1)	$E = 5.212 \times 10^{-2}$	$E = 3.823 \times 10^{-3}$	$E = 3.791 \times 10^{-3}$
Nonlinear (Fig. 2)	$E = 1.213 \times 10^{-3}$	$E = 1.740 \times 10^{-3}$	$E = 1.128 \times 10^{-3}$

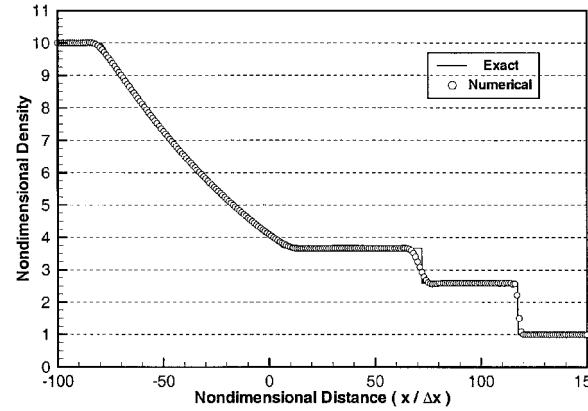

Jameson et al.[7] model

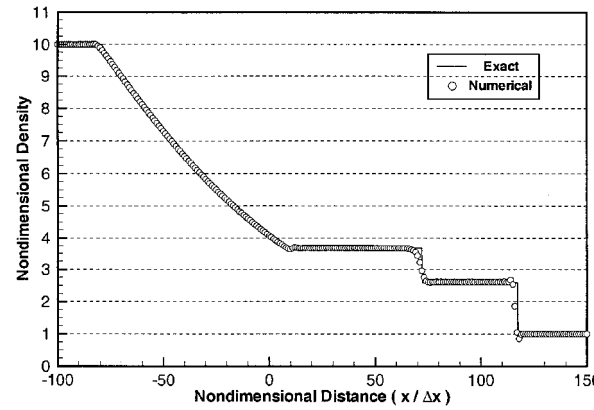

Tam et al.[12] model

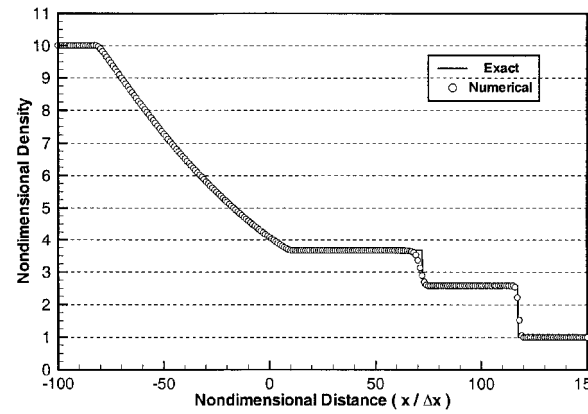

ANAD model

Fig. 2 Computation of shock-tube simulation (density profile).

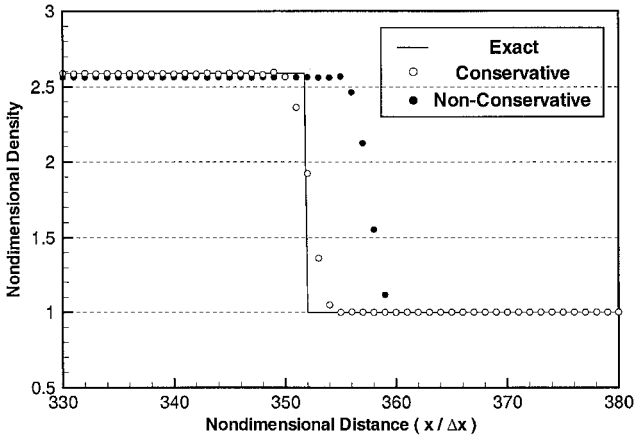

Fig. 3 Comparison between the conservative and nonconservative ANAD models (density profile).

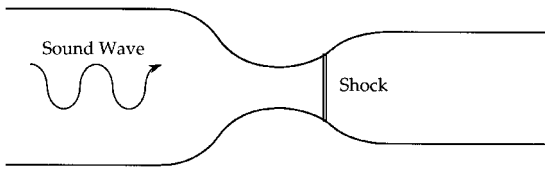

Fig. 4 Schematic diagram for computations of shock–sound interaction in a transonic nozzle.

C. Quasi-One-Dimensional Computation

For quasi-one-dimensional computations, problem 2 in category 1 in Ref. 20 is solved in the present study. This problem is assigned for simulating the shock–sound interactions in a transonic nozzle. The schematic diagram of the problem is illustrated in Fig. 4. All quantities are nondimensionalized by the upstream values: length scale equals D_{inlet}, density scale equals ρ_{inlet}, velocity scale equals c_{inlet}, pressure scale equals $\rho_{\text{inlet}} c_{\text{inlet}}^2$, and timescale equals $D_{\text{inlet}}/c_{\text{inlet}}$, where D is the nozzle height and c is the speed of sound. The domain is $-10 \le x \le 10$, and the area of the nozzle is given by

$$A(x) = \begin{cases} 1.0 - 0.661514\exp[-(\ell n 2)(x/0.6)^2], & x \le 0 \\ 0.536572 - 0.198086\exp[-(\ell n 2)(x/0.6)^2], & x \le 0 \end{cases}$$

At the inflow boundary, the inlet Mach number is $M_{\text{inlet}} = 0.2006533$, and the magnitudes of acoustic perturbations for the density, pressure, and velocity are equally $\varepsilon = 1 \times 10^{-5}$ times the ambient values of their scales at the inlet plane. The frequency of perturbations is $\omega = 0.6\pi$. The mean pressure at the outflow boundary is set to create a shock: $p_{\text{exit}} = 0.6071752\gamma p_{\text{inlet}}$.

For the quasi-one-dimensional computations, Eq. (22) is solved. The ANAD model captures the shock, removes the spurious oscillations, and helps the schemes to reach steady mean solutions with little damping on the acoustic waves. The number of grid points used is 251, and the grids are clustered near the nozzle throat. The time step used is determined by a CFL condition with Courant number of 0.9. The convergence criterion for steady state is that the maximum value of the residual, defined as $|\rho^{(n+1)} - \rho^{(n)}|/\rho^{(n)}$, is below 1×10^{-15}, which is the order of machine error. After the steady state is reached the acoustic perturbation starts at the inlet plane, and the periodic oscillatory state with constant magnitudes is achieved, during which 25 wavelengths are produced.

The error residual history for the steady mean solutions is represented in Fig. 5, which shows a fair convergence rate to the steady state without any convergence acceleration technique. The computation time to obtain the steady mean solutions is 23.8 s through 16,000 operations using Intel's 400-MHz Celeron CPU, and the fraction of computation time used by the ANAD model is 31.3% in this case. The steady mean solutions are represented in Fig. 6, where it is shown that the numerical solutions are in good agreement with the analytic solutions. The value of adaptive control constant calculated by Eq. (25) is $\kappa = 5.708$ when the steady state is reached before

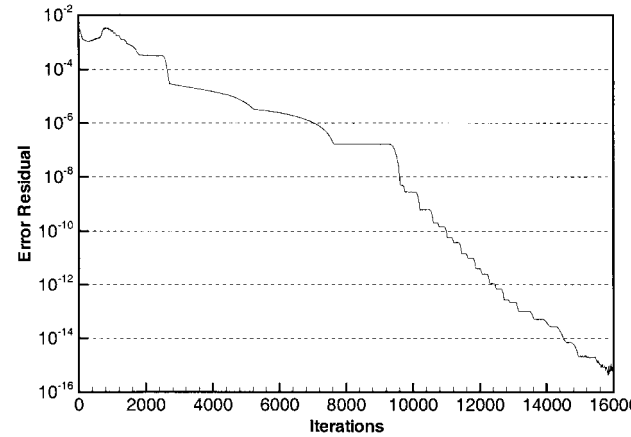

Fig. 5 Error residual history for steady mean solutions in quasi-one-dimensional transonic nozzle computation.

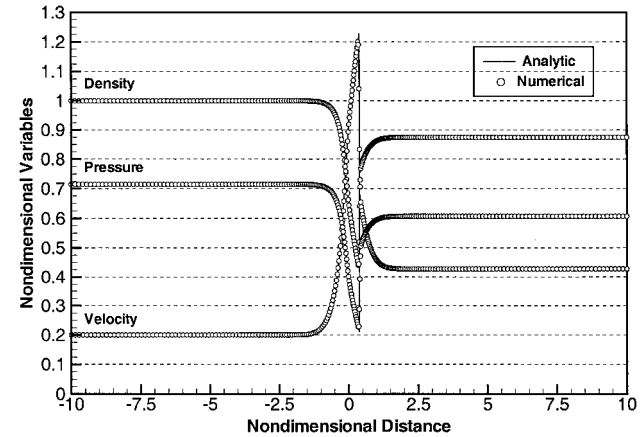

Fig. 6 Steady mean solutions compared with analytic solutions in quasi-one-dimensional transonic nozzle computation.

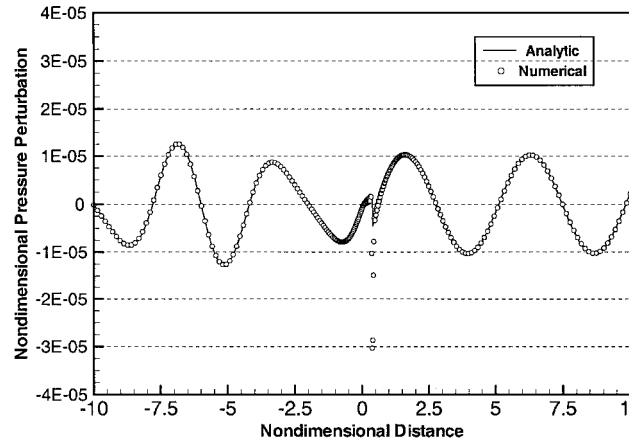

Fig. 7 Distribution of pressure perturbations at a start of the period of inlet perturbation in quasi-one-dimensional transonic nozzle computation.

the inlet perturbation starts. The distribution of pressure perturbations $[p(x) - \bar{p}(x)]$ at the start of the period of the inlet perturbation are expressed in Fig. 7, where the interference between the incident and reflected waves at the upstream region, the shock–sound interaction at the throat, and the transmitted waves at the downstream region are shown well. There appears a peak at the shock position in Fig. 7, which is from the shock oscillation. The steep gradient at the shock front induces large pressure perturbation for small acoustic disturbances. Ideally, the shock thickness is zero, the gradient is infinite, and the peak perturbation will approach the difference of mean

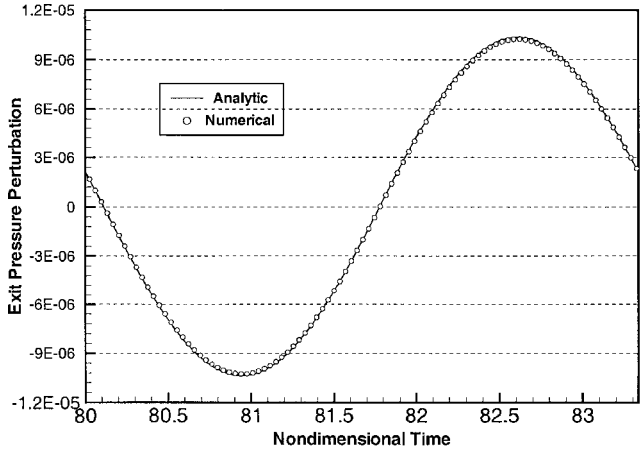

Fig. 8 Exit pressure perturbation signal through one period in quasi-one-dimensional transonic nozzle computation.

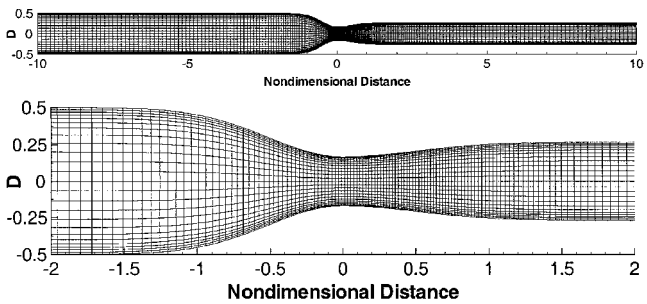

Fig. 9 Grid mesh system for two-dimensional transonic nozzle computation: entire view and zoomed view.

pressures before and after the shock. Some numerical oscillations still show near the shock in Figs. 6 and 7; however, these are small enough not to contaminate the acoustic data. The exit pressure signal through one period is represented in Fig. 8. The results in Fig. 7 and 8 are also in good agreement with the analytic solutions. The accuracy of the quasi-one-dimensional ANAD model is properly validated.

D. Two-Dimensional Computation

The same problem described in the preceding subsection is solved in two dimensions, which is more realistic, for the validation of the multidimensional ANAD model. For the two-dimensional transonic nozzle computations, Eq. (26) is solved. The numbers of grid points used are 251 in the x direction and 25 in the y direction (251×25), where the distribution of x-directional grid points are the same as that of the quasi-one-dimensional computation. The Courant number and the convergence criterion for steady state are also the same as those of the quasi-one-dimensional computation. After the steady state is reached, the acoustic perturbation starts at the inlet plane, and the periodic oscillatory state with constant magnitudes is achieved, during which 25 wavelengths are produced, just like in the quasi-one-dimensional case.

The grid meshes are represented in Fig. 9. The error residual history for the steady mean solutions is represented in Fig. 10. Convergence rate in the two-dimensional case is much slower than in the quasi-one-dimensional case, mainly because of the wall boundary conditions that reflect all of the waves perfectly into the computational domain. The canceling-the-residual technique[19] is implemented for convergence acceleration after 140,000 operations in Fig. 10, which saves much computational time in this case. The computation time to obtain the steady mean solutions is 330.1 min through 200,000 operations using Intel's 400-MHz Celeron CPU, and the fraction of computation time used by the ANAD model is 24.3% in this case, which is smaller than that in the quasi-one-dimensional case by 7%. The contours of steady mean solutions are represented in Fig. 11. The steady mean solutions on the nozzle centerline ($y = 0$) are represented in Fig. 12, where it is shown that

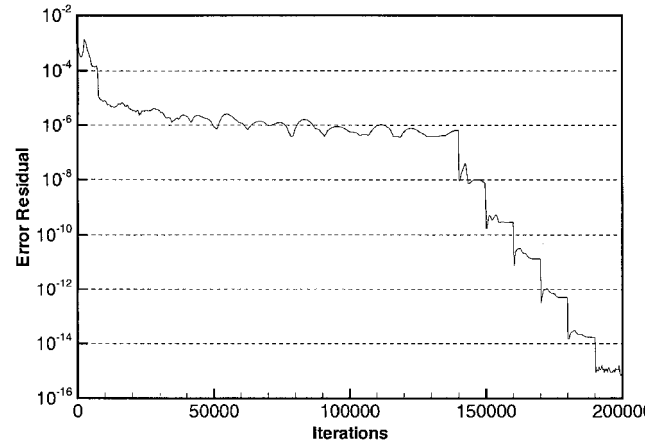

Fig. 10 Error residual history for steady mean solutions in quasi-one-dimensional transonic nozzle computation.

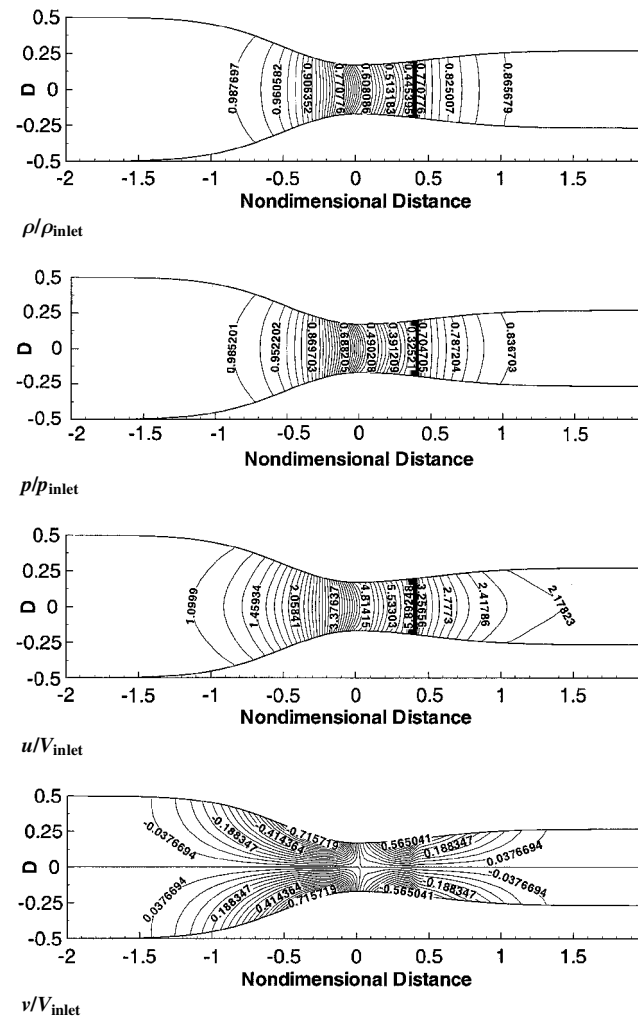

Fig. 11 Contours of steady mean solutions in two-dimensional transonic nozzle computation (41 levels).

the numerical solutions are in good agreement with the quasi-one-dimensional analytic solutions, just as in Fig. 6. The values of the adaptive control constant calculated by Eq. (31) are $\kappa = 5.714$ in the x direction and $\kappa = 1.881$ in the y direction at the center of the nozzle throat (x and $y = 0$) when the steady state is reached before the inlet perturbation starts. The distribution of pressure perturbations $[p(x) - \bar{p}(x)]$ on the nozzle centerline ($y = 0$) at a start of the period of inlet perturbation is expressed in Fig. 13, which corresponds to the quasi-one-dimensional result of Fig. 7. The peak perturbation and the small oscillations at and near the shock resemble those in

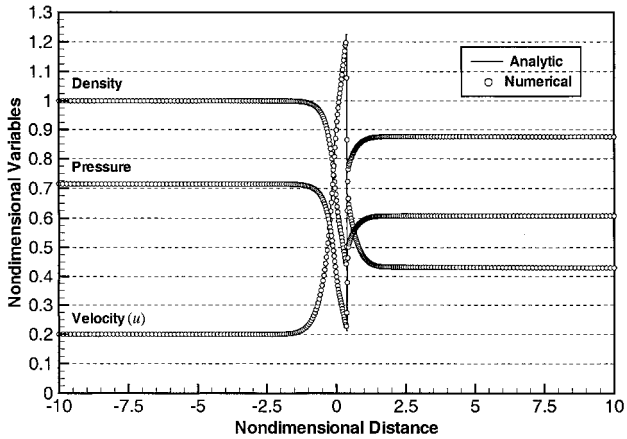

Fig. 12 Steady mean solutions compared with analytic solutions in two-dimensional transonic nozzle computation.

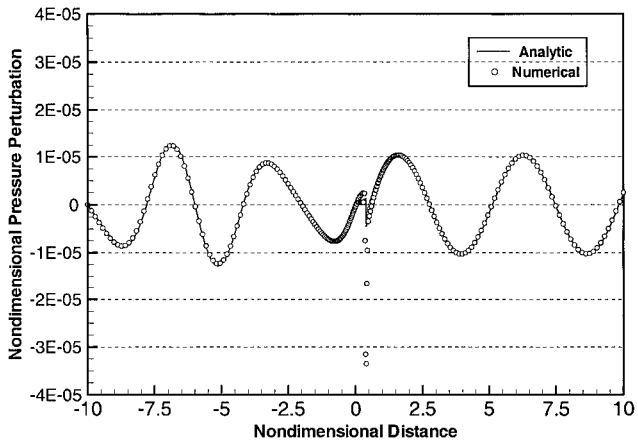

Fig. 13 Distribution of pressure perturbations at a start of the period of inlet perturbation in two-dimensional transonic nozzle computation.

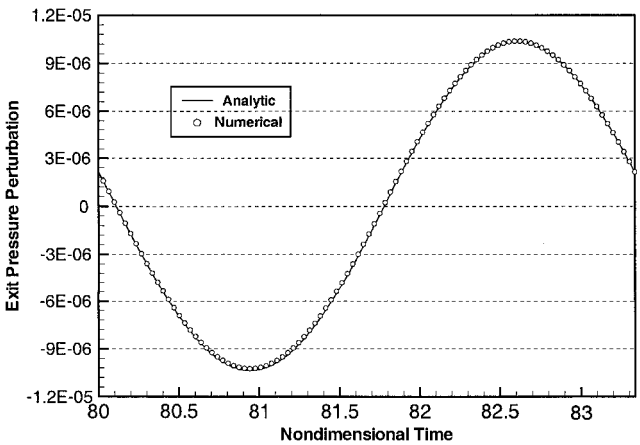

Fig. 14 Exit pressure perturbation signal through one period in two-dimensional transonic nozzle computation.

the quasi-one-dimensional case. The exit pressure signal at the center ($y = 0$) through one period is represented in Fig. 14, which is equivalent to that of the quasi-one-dimensional result of Fig. 8. The accuracy and feasibility of the multidimensional ANAD model in the generalized coordinates are properly validated and investigated within the present test problems.

VI. Conclusions

The ANAD model is presented for the numerical stability and convergence of CAA with high-order and high-resolution schemes. The ANAD model has excellent shock-capturing and background smoothing terms, and it scarcely dissipates the linear acoustic waves. The conservative form of the background smoothing term provides the accurate locations and propagation speeds of the shock waves. The adaptive control constant is devised to determine the optimum values of overall dissipation magnitude automatically, according to flow conditions and grid meshes. The one-, quasi-one-, and two-dimensional formulations of the ANAD models are successfully accomplished, and their applications to the actual Euler computations of the benchmarking problems provide high-quality nonlinear shock and linear acoustic wave solutions. Further tests and applications to various problems are expected to be helpful in validating the generality and feasibility of the ANAD model for CAA in the future studies.

References

[1]Kim, J. W., and Lee, D. J., "Optimized Compact Finite Difference Schemes with Maximum Resolution," *AIAA Journal*, Vol. 34, No. 5, 1996, pp. 887–893.

[2]Kim, J. W., and Lee, D. J., "Numerical Simulation of Nonlinear Waves Using Optimized High-Order Compact Schemes," *Computational Fluid Dynamics Journal*, Vol. 5, No. 3, 1996, pp. 281–300.

[3]Kim, J. W., and Lee, D. J., "Implementation of Boundary Conditions for Optimized High-Order Compact Schemes," *Journal of Computational Acoustics*, Vol. 5, No. 2, 1997, pp. 177–191.

[4]Lele, S. K., "Compact Finite Difference Schemes with Spectral-Like Resolution," *Journal of Computational Physics*, Vol. 103, No. 1, 1992, pp. 16–42.

[5]Tam, C. K. W., and Webb, J. C., "Dispersion-Relation-Preserving Finite Difference Schemes for Computational Acoustics," *Journal of Computational Physics*, Vol. 107, No. 2, 1993, pp. 262–281.

[6]Tam, C. K. W., "Computational Aeroacoustics: Issues and Methods," AIAA Paper 95-0677, 1995.

[7]Jameson, A., Schmidt, W., and Turkel, E., "Numerical Simulation of the Euler Equations by Finite Volume Methods Using Runge–Kutta Time Stepping Schemes," AIAA Paper 81-1259, 1981.

[8]Jameson, A., "Transonic Aerofoil Calculations Using the Euler Equations," *Numerical Methods in Aeronautical Fluid Dynamics*, Academic Press, New York, 1982.

[9]Pulliam, T. H., and Steger, J. L., "Recent Improvements in Efficiency, Accuracy, and Convergence for Implicit Approximate Factorization Algorithms" AIAA Paper 85-0360, 1985.

[10]Pulliam, T. H., "Artificial Dissipation Models for the Euler Equations," AIAA Paper 85-0438, 1985.

[11]Swanson, R. C., and Turkel, E., "Artificial Dissipation and Central Difference Schemes for the Euler and Navier–Stokes Equations," AIAA Paper 87-1107, 1987.

[12]Tam, C. K. W., Webb, J. C., and Dong, Z., "A Study of the Short Wave Components in Computational Acoustics," *Journal of Computational Acoustics*, Vol. 1, No. 1, 1993, pp. 1–30.

[13]Tam, C. K. W., and Shen, H., "Direct Computation of Nonlinear Acoustic Pulses Using High-Order Finite Difference Schemes," AIAA Paper 93-4325, 1993.

[14]Lockhard, D. P., and Morris, P. J., "Radiated Noise from Airfoils in Realistic Mean Flows," *AIAA Journal*, Vol. 36, No. 6, 1998, pp. 907–914.

[15]LeVeque, R. J., "Conservative Methods for Nonlinear Problems," *Numerical Methods for Conservation Laws*, 2nd ed., Birkhäuser Verlag, Boston, 1992, pp. 122–135.

[16]Thompson, K. W., "Time Dependent Boundary Conditions for Hyperbolic Systems II," *Journal of Computataional Physics*, Vol. 89, No. 2, 1990, pp. 439–461.

[17]Poinsot, T. J., and Lele, S. K., "Boundary Conditions for Direct Simulations of Compressible Viscous Flow," *Journal of Computational Physics*, Vol. 101, No. 1, 1992, pp. 104–129.

[18]Kim, J. W., and Lee, D. J., "Generalized Characteristic Boundary Conditions for Computational Aeroacoustics," *AIAA Journal*, Vol. 38, No. 11, 2000, pp. 2040–2049.

[19]Tam, C. K. W., Shen, H., Kurbatskii, K. A., Auriault, L., Dong, Z., and Webb, J. C., "Solutions to the Benchmark Problems by the Dispersion-Relation-Preserving Scheme," *ICASE/LaRC Workshop on Benchmark Problems in Computational Aeroacoustics*, NASA CP 3300, 1995, pp. 149–171.

[20]Kim, J. W., and Lee, D. J., "Adaptive Nonlinear Artificial Dissipation Model for Computational Aeroacoustics," *Proceedings of Third CAA Workshop on Benchmark Problems*, NASA CP-2000-209790, 2000, pp. 235–245.

P. J. Morris
Associate Editor